Acceleration of Particle-In-Cell Simulations using Sparse Grid Algorithms. I. Application to Dual Frequency Capacitive Discharges

L. Garrigues,[1] M. Chung-To-Sang,[1] G. Fubiani,[1] C. Guillet,[1,2] F. Deluzet,[2] and J. Narski[2]
[1)] *LAPLACE, Université de Toulouse, CNRS, INPT, UPS, Toulouse, France*
[2)] *Université de Toulouse, UPS, INSA, UT1, UTM, Institut de Mathématiques de Toulouse, CNRS, Institut de Mathématiques de Toulouse, UMR 5219, 31062 Toulouse, France*

(*Electronic mail: laurent.garrigues@laplace.univ-tlse.fr)

(Dated: 16 July 2024)

The use of sparse particle-in-cell (PIC) algorithms to accelerate the standard explicit PIC scheme has recently been successfully applied in the context of single-frequency capacitively coupled plasma discharges [Garrigues *et al.*, Journal of Applied Physics **129**, 153303 (2021)]. We have extended the sparse PIC scheme to model dual-frequency capacitive discharges. Comparisons between standard and sparse PIC algorithms show that the plasma properties as well as the electron and ion distribution functions can be retrieved with a maximum error of 2 %. This work opens the interest of using the sparse PIC algorithm to perform 2D and 3D simulations under real operating conditions of capacitively coupled plasma discharges.

I. INTRODUCTION

The use of radio frequency (RF) capacitively coupled plasmas (CCP) in the context of processing techniques for the microelectronics industry (sputtering, etching, deposition, etc.) has become unavoidable[1–3]. Such technology has been operating at a single RF frequency f_{RF} (most of the time 13.56 MHz) with difficulties to achieve the technology requirements with independent control of suitable high-density plasmas and ion fluxes and ion energies bombarding the substrate. This is due to the increase of the plasma density which scales with ${f_{RF}}^2$ (Ref.2). As a consequence, the ratio between the ion transit time and the RF period $\tau_{\rm ion}/\tau_{\rm RF} >> 1$, and ion-neutral collisions such as charge exchange processes reduce the energy gained by the ions in the sheath and modify the shape of the ion energy distribution functions with the formation of peaks at given energies (see e.g. Ref.4). Dual-frequency RF plasma discharges have been introduced to separately control ion flux and energy at the wafer surface. They are based on a much higher frequency than the other and the reason is related to the separation of the role of electrons and ions in the discharge. While the higher frequency (and voltage) is chosen to achieve high plasma density by controlling the ionization of the gas, the lower frequency is suitable to control the ion energy[5,6]. The high frequency is typically in the range of 13.56 – 160 MHz, while the low frequency is between 0.5 and 13.56 MHz. The RF voltages typically vary between 100 and 600 V with the low frequency voltage being significantly higher than the high frequency voltage[7].

The fluid approach, including its extension to two-dimensional geometry, has played an important role in the global understanding of CCP, but it suffers from limitations in capturing the non-local and non-equilibrium effects in a self-consistent approach[7]. In addition, the non-Maxwellian shape of the electron energy distribution function (EEDF) in CCP discharges makes the use of the particle-in-cell Monte Carlo collision (PIC-MCC) approach more appropriate. The electrostatic approximation is used as long as the excitation wavelength is larger than the electrode radius, which means that electromagnetic effects are negligible and charge motion only affects the electrostatic electric field profile solution of Poisson's equation. One-dimensional (1D) approaches to calculate the spatial plasma dependence between the grounded and RF electrode have been widely used for single[5,6,8,9], dual[10,11] and both single and dual[12] frequencies. To capture the two-dimensional (2D) effects of the reactor, 2D simulations have been performed (e.g., Refs.13 and 14 for dual-frequency CCP). Nevertheless, 2D explicit PIC simulations are time-consuming, and alternative methods based on the implicit approach coupled with parallelization techniques have been employed[15,16]. Graphic Processing Unit (GPU) machines have also been used to reduce the computation time[17,18].

The PIC scheme couples Lagrangian particles, representing a discretization of the distribution functions in phase space, with an Eulerian grid to compute Maxwell's equations (limited to Poisson's equation for CCP discharges). A first criteria to avoid finite-grid instabilities associated with the PIC algorithms imposes to resolve the electron Debye length. The explicit formulation of the electrostatic PIC scheme takes advantage of a simple implementation of the algorithm accompanied by a limited memory size for the particle data, but is requires the need to resolve the reciprocal electron plasma frequency for the time step to conserve a stable and accurate scheme[19–22].

The main source of error associated with PIC approaches is the statistical error introduced by using a finite number of numerical particles to sample the distribution functions. The total number of particles scales as N^d, where N is the number of unknowns (grid nodes) and d is the dimension. For large numbers N and d, the total number of particles can reach very high numbers, which increases the demand on computational and memory resources. The use of sparse grid algorithms with the so-called combination technique aims to break this dependency. The advantage of combining sparse and PIC approaches is the reduction of the total number of particles for a precision of the same order as in the standard PIC algorithm[23,24]. The interest of the method has been demonstrated for basic test cases in 2D (linear[23,24], non-linear Landau damping[24], the Diocotron instability[23]) and in 3D

(linear[25] and non-linear Landau damping[23], the Diocotron instability[25,26], the Penning trap[27]). The implementation of the sparse PIC method in the context of low temperature plasmas has been shown in the work of Garrigues *et al.*[28,29]. The motivation of this paper is to perform benchmark simulations between standard and sparse electrostatic PIC simulations in the context of dual-frequency CCP discharges. In the rest of the paper, we return to sparse PIC approaches in section II. The dual-frequency RF modeling conditions are introduced in section III. Section IV is devoted to simulation comparisons between standard and sparse PIC schemes and discussion. Finally, section V summarizes the main conclusions.

II. SPARSE-PIC APPROACHES

In this section, we discuss the main sources of error due to the combination technique when the quantities are reconstructed on the computational grid, namely the grid-based error (Section II A). The subgrid constructions, extended to the case of a rectangular computational domain, are reported in section II B. The sparse PIC cycle is presented in section II C, while the strategy of sparse PIC implementation is described in section II D.

A. Grid based error related to the sparse PIC algorithms

Aside the error due to the time discretization of the motion equation using the standard Leapfrog algorithm[19,20] $[O(\Delta t^2)]$, the source of errors in PIC algorithms are due to the grid-based error and the statistical or particle sampling error related to the mean number of particles per cell used in the simulations[23,24,27]. Compared to the standard PIC algorithms, the introduction of the sparse grid approach offers an undeniable interest in the reduction of the statistical error. For the same average number of particles per cell as in the standard approach, the reduction of the number of cells accumulated on each of the subgrids results in a reduction of the total number of particles. However, the sparse PIC approach suffers from a larger grid error compared to the standard PIC algorithm. This is due to the anisotropic grids with coarser mesh resolution[23,24,27]. The numerical analysis of the grid-based detailed in ref. 24 and 27 shows that the contribution of the cross (off-axis) derivative terms can become dominant (with respect to the axis derivative terms). The reduction of the error in the mixed derivative terms is accompanied by an increase in the error for the terms along the axis. However, this error is still negligible. One can reduce the grid-based error by using an appropriate coordinate system and grid construction, e.g. aligned with the magnetic field lines in the case of the study of magnetized plasmas[23]. Nevertheless, this method has not yet been carried out and further analysis is needed regarding the consequences on the error associated with the statistical noise.

Muralikrishnan *et al.*[27] have proposed a modification of the classical sparse PIC algorithm using a truncated approach. This method aims to use a smaller number of subgrids, but with a finer mesh resolution, in order to reduce the grid-based error when combining the solution. This method has been extended in the work of Deluzet *et al.*[24] with the so-called offset method, which takes advantage of the truncated method with a more subtle way to manage the subset of subgrids. However, as a trade-off, the particle sampling error increases, but it can be controlled by increasing the total number of particles to keep the number of particles per cell constant. In practice, two tuning parameters are used to choose the number of subgrids and the mesh resolution on each of the subgrids.Very importantly, like the classical sparse PIC approach, momentum conservation is preserved with the offset sparse PIC approach[24]. We illustrate the construction of the subgrids with the offset method in a simple 2D case in section II B. The classical sparse PIC algorithm is obtained by setting these two parameters to zero. Finally, the algorithm in the offset sparse PIC methods is very similar to the classical sparse PIC, making its implementation very easy. The potential of the truncated and offset methods has been demonstrated in the studies of the diocotron instability in 2D[24,27] and 3D[25], and the 3D Penning trap[27].

B. Component grids construction and combination technique with the offset method

We illustrate in a 2D example the construction of sparse grids when the offset method is used. We have adopted the terminology of *component grid* proposed by Deluzet *et al.*[25] to define the anisotropic subgrids with coarser resolution. The initial Cartesian grid with a constant mesh width is called the *regular grid*. We illustrate the construction of the sub-grids for a regular grid with a number of nodes equal to 2^n+1 in each direction and with a uniform mesh width in both directions $h_x = h_y = h = 2^{-n}$ for $n = 4$. The grid-based error is handled by the integer parameters l^0 and l^1. While the l^0 parameter is used to control the grid-based error in off-axis directions, the l^1 parameter controls the number of anisotropic grids to discard for a better approximation in the combination technique. The construction of the component grids for the offset method can be generalized from the work of e.g. Ref. 23 and 28. Let k and m be the row and column indices of the component grids. There are two sets of component grids for 2D sparse methods. A component grid is defined by a pair (k,m) whose integers satisfy $k+m = n+l^0-l^1+1$ for a positive contribution and $k+m = n+l^0-l^1$ for a negative contribution to the reconstruction of the solution by the recombination technique, and with $(k,m) > l^0$.

This is illustrated in Fig.1 for the offset and classical approaches. The number of component grids is $2(n-l^0-l^1)-1$. When $l^0 = 0$ and $l^1 = 0$ (at the bottom of Fig.1), the component grids are the same as those ones given by the classical sparse PIC approach. Note the strong anisotropy of the component grids G_{41}, G_{14}, G_{31}, and G_{13}. When the truncated method is used, for $l^0 = 1$, while keeping $l^1 = 0$ (center of Fig.1), the number of the components grids is reduced and the mesh width in both directions is thinner, reducing the grid-based error in off-axis directions. If both l^0 and l^1 are set to 1

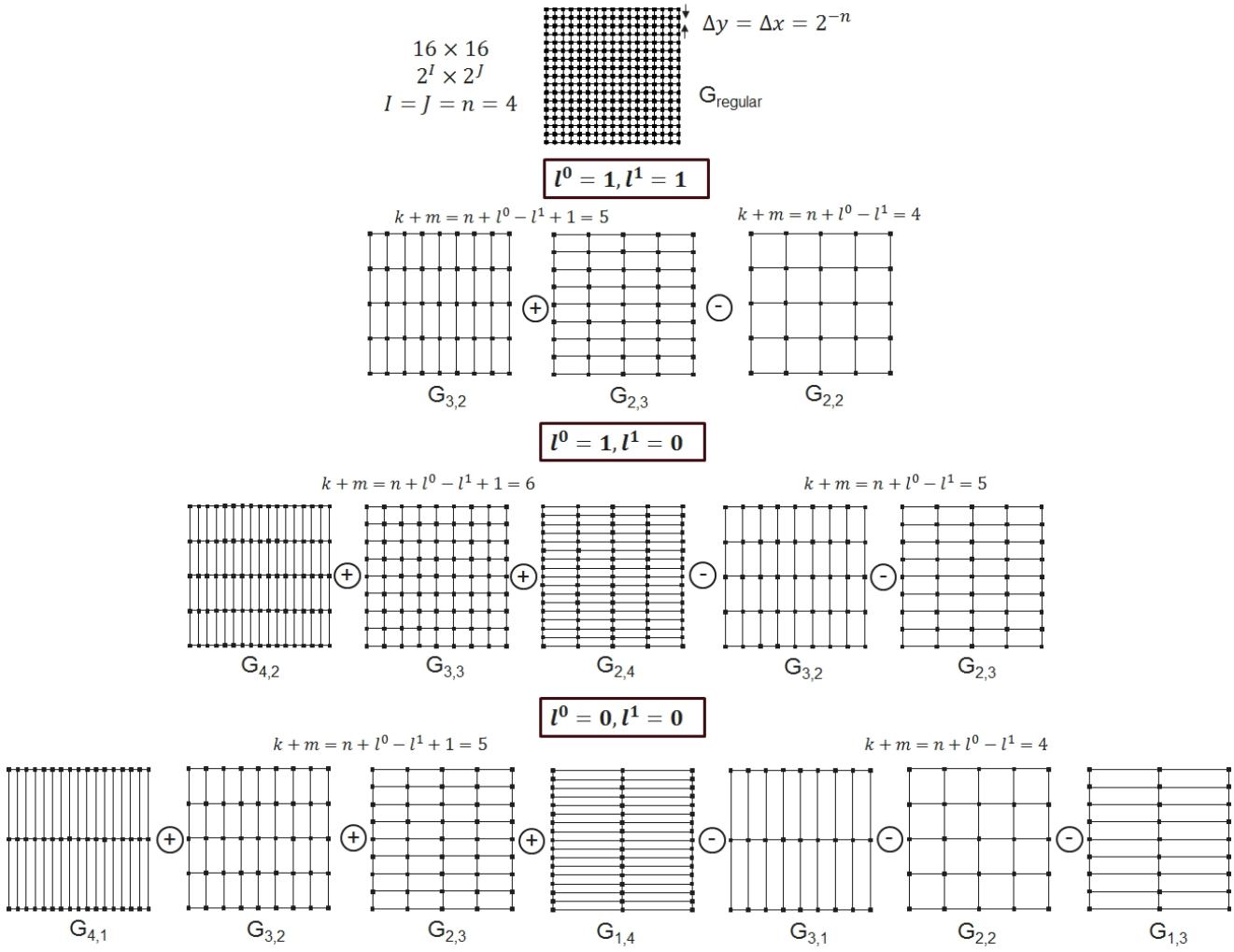

FIG. 1. Component grids construction for a regular grid $2^I \times 2^J$ with $I = J = n = 4$, for the (top) offset with $l^0 = l^1 = 1$, (center) offset with $l^0 = 1$ and $l^1 = 0$ and, (bottom) classical ($l^0 = l^1 = 0$) sparse PIC approaches. Each of the component grid is noticed $G_{k,m}$ where k and m are tow integers.

(top of Fig.1), the grids with largest anisotropy are discarded.

When considering the truncated method, the total number of cells, which is the sum of all the cells of the component grids, is larger. To maintain the same statistical error, the total number of particles N_p^{OS} must be increased. Noting that P_c is the number of particles per cell and N_p is the total number in all cells, Deluzet *et al.*[24] generalized the calculation of P_c for the classical sparse PIC algorithm given by Ricketson *et al.*[23] including the offset method:

$$N_p^{OS} = N_p^S \frac{2^{N_2}(3N_1 - 1)}{2^n(3n - 1)} \tag{1}$$

where the total number of particles in the standard sparse PIC is noticed N_p^S, and N_2 and N_1 are given by $N_2 = n + l^0 - l^1$ and $N_1 = n - l^0 - l^1$. For the same N_p, the number of particles per cell increases with l^0.

We define i and j the indices of the row and column of the nodes of the regular grid. For any set U computed for any k and m of the components grids, the approximation of the same set at the position defined by i and j on the regular grid is given by the so-called combination technique introduced in the context of sparse PIC simulation, first by Ricketson *et al.*[23] and extended with the offset method by Deluzet *et al.*[24].

$$U_{i,j} = \sum_{k+m=N_2+1} U^{k,m} - \sum_{k+m=N_2} U^{k,m} \tag{2}$$

We have extended the construction of the component grids for a rectangular regular grid in the case of the classical sparse approach but it can be easily generalized to the offset method. In the example shown in Figure 2, we have taken the example of the domain of $2^{n_1} \times 2^{n_2}$ with $n_1 = 3$ and $n_2 = 4$ (the mesh width is still uniform but with a larger distance along the y direction, $n_2 > n_1$). The component grids are now constructed such that, for any pair of coordinates (k,m), the first set of grids are given by $k + m = n_2 + 1$ and the second set of grids is given by $k + m = n_2$ with $m > n_2 - n_1$. In this configuration,

the grid error is decomposed into a dominant off-axis derivative term scaling as $O(n_2 h_{n_2}^2)$ and two negligible axis derivative terms scaling as $O(h_{n_1}^2)$ and $O(h_{n_2}^2)$, where $h_{n_1} = 2^{-n_1}$ and $h_{n_2} = 2^{-n_2}$. The off-axis derivative term scaling as $O(n_1 h_{n_1}^2)$ is negligible compared to $O(n_2 h_{n_2}^2)$ because $(n_1 < n_2)$. For an equal number of P_c (and equal statistical error) between the standard and sparse PIC algorithms, the calculation of the total number of particles N_p^S with the sparse approach (when $n_2 > n_1$) is given by:

$$N_p^S = N_p \frac{(3n_2 - 7)}{2^{n_1}} \tag{3}$$

Finally, the relation for the combination technique is still given by Eq. (2).

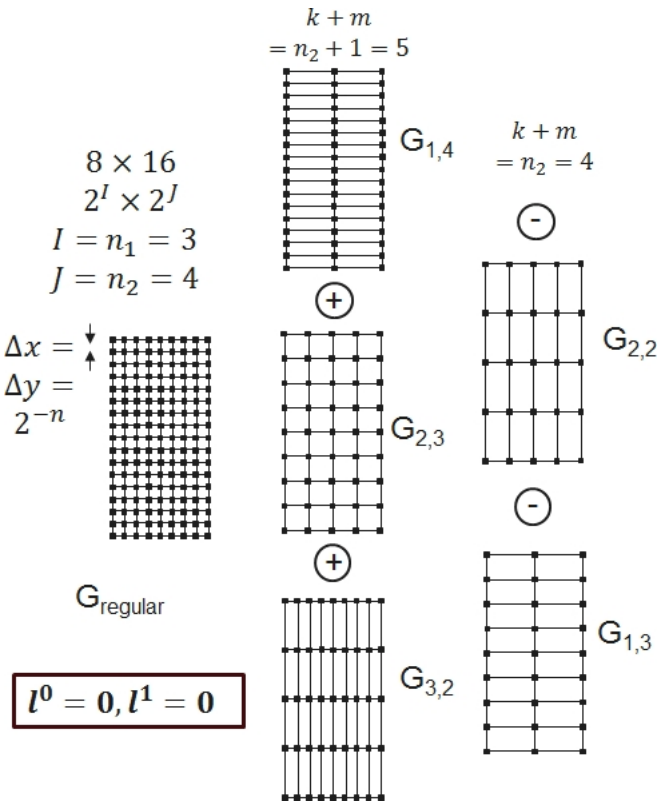

FIG. 2. Component grids construction for a rectangular regular grid $2^I \times 2^J$ with $I = n_1 = 3$ and $J = n_2 = 4$, for the classical sparse PIC approach ($l^0 = l^1 = 0$).

C. PIC cycle revisited for sparse algorithms

As in the standard PIC approach[19,30,31], the sparse PIC algorithm can be subdivided into different tasks. In figure 3 we show the PIC cycle rewritten for the sparse approach. The integration of the charged particle trajectories to update velocities and positions is done with the standard leapfrog scheme[32]. The injection and loss processes for the particles at the boundaries and/or in the volume when a source term is imposed are the same as in the standard PIC approach. Collisions, if any, are treated using the Monte Carlo null-collision technique. An estimate of the maximum collision frequency at the beginning of the simulation leads to the calculation of a fictive collision frequency that is constant and independent of the charged particle velocities. This method is convenient because the collision frequency in low-temperature plasmas is much smaller than the inverse of the plasma frequency. The collisions are performed once per PIC cycle. This method has been efficiently adapted to PIC simulations by reducing the sampling of charged particles potentially colliding during a time step from the estimate of the fictive collision frequency[31]. Random generator processes are then used to determine the probability of real events, new velocities, and the eventual generation of particles when ionization processes take place.

The changes to the standard PIC algorithm start with the assignment of the charged densities at the nodes to compute the electric potential profile. In the Sparse PIC algorithms, the charged densities at each of the nodes of each of the component meshes are computed using the common bi-linear (cloud-in-cell) weighting scheme[19,20]. The calculation of the electric potential can now be done in several ways. One can use the combination technique to compute the charge densities on the initial Cartesian grid and then compute the electric potential on the initial computational domain[24,27] (not shown in Fig.3). In this approach, the sparse technique serves only to filter the noise, reducing the statistical error in the calculation of the charged particle densities. We did not consider this option for two reasons. The first is that the detailed numerical analysis has shown that the recombination of the charged densities is not guaranteed to be positive (although no real problem has been pointed out by Muralikrishnan *et al.*[27], but further analysis is needed).

The second and most important point is that resolving Poisson's equation on the Cartesian grid (as in the standard PIC algorithms) is expensive. We have chosen to deposit the charges on each of the nodes of each of the component grids and to solve Poisson's equation on each of them. This approach significantly reduces the computational time, with a gain that is roughly proportional to the ratio between the total number of grid nodes on the uniform Cartesian grid compared to the total number of grid nodes on all the component grids. In addition, the charge densities computed at each of the component grid nodes are positive by construction. For the rest of the PIC cycle, we have implemented two algorithms from the literature.

In the first algorithm (left path of Fig.3), called PIC-HSg for sparse PIC discretized on the hierarchical component grids[23,24] (and PIC-OHSg for the offset sparse PIC method), after solving Poisson's equation on each of the component grids, the electric field at each node of each of the component grids is calculated from the electric potential profile with a second-order differential scheme as in the standard PIC approach. The bi-linear weighting scheme is used to interpolate the electric field at the particle location on each of the component grids, and after applying the combination technique [eq.(2)], it gives the calculation of the electric force at the particle locations. The scheme conserves the total charge and momentum, as in the standard PIC approach[24]. However, this ap-

proach requires a large number of operations, especially when using the bi-linear weighting scheme on each of the subgrids for all particles.

The second algorithm (right path of Fig.3) refers to the so-called nodal basis Sparse-PIC (noticed PIC-NSg in the literature[24,25] and in the rest of the study). By coherence, the use of this algorithm with the offset method will be noted PIC-ONSg. After calculating the electric potential on all the nodes of each of the component grids, the potential on all the nodes of the Cartesian grid is calculated using the combination technique [eq.(2)]. The electric field profile at the nodes of the Cartesian grid is computed using a second-order differential scheme. Finally, the electric force acting on the motion of the charged particles is interpolated at the particle positions with the bi-linear weighting scheme. However, this method loses the conservation of momentum property. The bi-linear weighting scheme used to assign the particle sources to the nodes of each of the component grids is not the same as the one used to perform the interpolation of the electric field at the particle positions. Applying this algorithm to the conditions of nonlinear Landau damping has shown that this error remains small and bounded, which is not a critical issue[24]. An extremely efficient method based on the hierarchical decomposition of the basis functions leads to a reduction in the complexity of the combination operations, reducing the computational time required to perform these operations[25]. This method is equivalent to the recombination of the electric potential profile from the profiles calculated on the component grids, but takes advantage of the reduction in the number of operations performed.

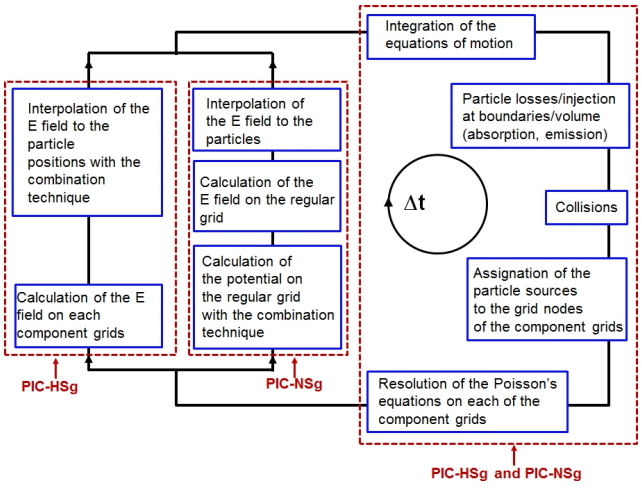

FIG. 3. Sparse PIC cycle with the PIC-HSg and PIC-NSg schemes.

D. Implementation strategy

The strategies for optimization and parallelization are the same as those used in the previous works of Garrigues *et al.* (see 28 and 29 and references therein). In summary, the common part of the PIC cycle between standard and sparse PIC methods is based on 1) hybrid parallelization (using message passing interface (MPI) libraries between nodes and shared memory - using Open Multi-Processing (OpenMP) programming with FORTRAN) between cores, and 2) the particle decomposition technique, where the entire computational domains of the component grid (whose memory footprint is relatively small, see below) are seen by the threads of each core, each of which carries a subset of the initial distribution of particles. This strategy has demonstrated its strong speed-up scaling capability for 2D simulations.

Focusing on the specific steps related to the sparse PIC algorithm, Poisson's equations are solved in parallel on each of the OpenMP threads. The solution of Poisson's equation does not require much computational effort (see in ref. 28 and 29). Now, special attention was paid to the strategy for assigning the sources to the grid nodes of the component grids (and also the interpolation of the electric field at the particle location for the PIC-HSg algorithm) for the memory management policies. Deluzet *et al.*[25] have implemented and tested two methods. In the first method, the contribution of a particle to each of the component grids is made before proceeding to the next particle. The second method does the opposite, making the contributions of all particles with one component grid before moving onto the next. For 3D simulations on shared memory architectures (both for CPU[25] and GPU[26]), the second method shows a quasi ideal scalability (due to the array size of the component grids that enters the cash level memory, allowing fast memory accesses). Accordingly, we implemented the second strategy.

III. DUAL FREQUENCY RF MODELING CONDITIONS

In the low-frequency power supply, the voltage varies from 400 to 600 V and the frequency is fixed at 2 MHz, while a variable high-frequency power supply is supplied, varying the frequency for a voltage in the range of 200-450 V. The overall sinusoidal waveform can be expressed as follows

$$V_T(t) = V_{HF}\sin(2\pi f_{HF}t) + V_{LF}\sin(2\pi f_{LF}t) \qquad (4)$$

where the subscripts HF and LF stand for high and low frequencies, respectively. Two configurations (cases) and associated computational domains have been tested, keeping the grid spacing along the x and y directions constant. Quasi-one dimensional simulations have been performed using periodic boundary conditions along the y direction. The inter-electrode gap is filled with the helium gas at a temperature of 300 K. The neutral density varies from 7×10^{20} m^{-3} to 2×10^{21} m^{-3} depending on the initial conditions and is kept constant during the simulations. The choice of the initial neutral density has been made to obtain plasma densities in the order of 10^{15} m^{-3} to perform simulations with a spatial resolution that guarantees the electron Debye length resolution with a maximum number of grid nodes of 256 for a length of 6.67 cm, while keeping acceptable computational times. Using the notations introduced in section II B, the sparse PIC simulations correspond to $n = 8$.

At time zero, a plasma density n_0 is prescribed, consisting of an equal number of electrons and singly charged ions. Particle positions are randomly initialized in the simulation domain. The initial velocities are sampled from Maxwellian distributions at given temperatures, 3 eV for the electrons and 0.026 eV for the ions. The left and right walls along the x direction are electrodes, the left one is grounded and the right one is supplied with the RF voltage according to Eq. 4 (Dirichlet boundary conditions). Along the y direction, periodic boundary conditions are applied. All charged particles colliding with the electrode walls are absorbed and the secondary electron emission processes are not considered. When periodic boundary conditions are applied, the particles that pass through the top (or bottom) plane are reinjected at the bottom (or top) with the same velocity components.

We assume that the plasma density is small enough (less than a few times 10^{17} m^{-3}) to neglect Coulomb collisions. Both electron-neutral and ion-neutral collision processes are considered with a limited number of reactions. For the electron-neutral collisions, the data set is taken from Biagi v7.1[33] considering elastic, one ionization and two excitation levels. Note that the appendix of Ref. 34 provides a complete set of tabulated cross sections. As in Refs. 28 and 34, the residual energy after an ionization event is shared equally between the primary and secondary electrons. The post-collision velocities are assumed to be isotropic in the center of mass. As in the formulation of Phelps[35], the ion-neutral collisions are approximated with an isotropic scattering process plus an anisotropic backscattering process (in the center of mass). The time step Δt is chosen to resolve the reciprocal electron plasma frequency. The frequencies used correspond to typical etching conditions[7] and $V_{HF} < V_{LF}$. The pressure range in the calculations varies from 5 to 60 Pa. The table I summarizes the input parameters used in the simulations.

TABLE I. Physical and initial numerical parameters for the benchmark.

Physical parameters	CASE A	CASE B
wall distance along x, L_x (cm)	6.7	6.7
wall distance along y, L_y (cm)	6.7	6.7
neutral density N (10^{21} m^{-3})	2	0.73
neutral temperature T_N (K)	300	300
HF frequency f_{HF} (MHz)	20	60
HF voltage V_{HF} (V)	450	200
LF frequency f_{LF} (MHz)	2	2
LF voltage V_{LF} (V)	600	400
Physical constants	**CASE A**	**CASE B**
electron mass m_e (10^{-31} kg)	9.11	9.11
ion mass m_i (10^{-27} kg)	6.69	6.69
Initial conditions	**CASE A**	**CASE B**
plasma density n_0 (10^{14} m^{-3})	6.4	10.5
electron temperature T_e (K)	35 000	35 000
ion temperature T_i (K)	300	300
Initial parameters	**CASE A**	**CASE B**
grid spacing Δx	$L_x/256$	$L_x/256$
grid spacing Δy	$L_y/256$	$L_y/256$
time step Δt (s)	$(800 f_{HF})^{-1}$	$(800 f_{HF})^{-1}$
initial number of particles per cell N_{pc}	130	130
Boundary conditions	**CASE A**	**CASE B**
left wall	grounded	grounded
right wall	RF	RF
top wall	periodic	periodic
bottom wall	periodic	periodic

IV. RESULTS AND DISCUSSIONS

This section compares the different algorithms, namely the standard PIC (PIC), the sparse grid with the hierarchical (PIC-HSg) and the nodal (PIC-NSg) combination techniques, for the three cases defined in the table I. For CASES A & B, the number of grid nodes is 256^2 for the standard PIC approach. For the sparse grid calculations, the level is $n = 8$. The extension of the PIC-HSg algorithm with the offset method (PIC-OHSg) is also shown for $l^0 = 3$ and $l^1 = 1$. For all calculations, the simulation time is 400 LF cycles and the averaging time is 20 LF cycles for CASE A and 40 LF cycles for CASE B. We conclude this section with a discussion focusing on error computation and the advantages of sparse PIC approaches for reducing computation time.

A. CASE A

For each computational case, the number of particles per cell is $N_{pc} = 130$ and the total number N_T is 8.52×10^6, 8.52×10^5, 8.52×10^5, and 1.67×10^6 for the PIC, PIC-HSg, PIC-NSg, and PIC-OHSg algorithms, respectively. In Fig.4a we show the time averaged profiles along x at the mid-distance along y of the charged particle densities. Regardless of the sparse PIC method, the profiles of the charged particle densities are identical to those of the PIC approach. In the context of dual-frequency capacitive discharges, the sparse PIC algorithm is able to correctly capture the sheaths in front of the electrodes. More interestingly, the electron energy distribution function (EEDF) averaged in both time and space and normalized such that a Maxwellian distribution would be a straight line is plotted in Fig.4b. Again, the EEDF profile is captured with a high precision of more than 6 orders of magnitude. The deviation between the standard and sparse PIC approaches appears at extremely high electron energies (tail of the distribution) for a very small number of particles. This is due to the reduced total number of particles used in sparse PIC. However, it does not affect the discharge characteristics. We notice that the shape deviates from a pure straight line and exhibits a super-thermal high energy tail. This has been at-

tributed to the non-local (stochastic) electron heating during the sheath oscillation[36–39].

One can estimate whether the non-local effect is responsible for the tail at high electron energies by comparing the electron-neutral collisions ν_{en}, the HF angular frequency ω_{HF}, and the transit time frequency of the electrons in the region of the potential drop (approximated by the sheath thickness - L_s) f_{trans}. For an electron velocity v_e, the latter can be approximated by $f_{trans} \sim v_e / L_s$. If $f_{trans} < \nu_{en}$, ω_{HF}, electrons heated during the RF cycle dissipate their energy locally in collisions, on the contrary, if $f_{trans} > \nu_{en}$, ω_{HF}, electrons are heated by a given numbers of the RF cycles before colliding with the neutral atoms. The average electron energy is consequently higher compared to the previous situation. For CASE A conditions, $\nu_{en} \sim 1.5 \times 10^8$ s^{-1} (almost constant), $\omega_{HF} \sim 2 \times 10^8$ rad.s^{-1}. For a sheath thickness of 2 cm (see below), the simple reasoning above shows that the non-local effects dominate for electron energies above 20 eV, which is consistent with the change in slope seen in Fig.4b.

It is rather instructive to plot the ionization source term, the number of electron-ion pairs per unit volume and time, as a function of time and space (on an LF cycle). Figures 5a and 5b show a comparison between standard and sparse PIC approaches. Note that only the PIC-HSg method is shown, the profile of the ionization source term for the PIC-NSg algorithm is the same. We have also superimposed the sheath edge in white on the same plot. As expected, the sheath edge varies under the influence of both frequencies. However, the thickness of the sheath is not constant for each RF oscillation and typically varies from 0 to 3 cm. The profile of the ionization source term is captured with very high accuracy by the sparse PIC algorithms. Almost no ionization takes place in the sheath and the maximum of ionization is concentrated in the center of the discharge and is almost constant in time. It is useful to remember that no secondary electron emission from the electrode surfaces under ion impact is included in the calculations. We probably miss the ionization events at the sheath edge under the acceleration of the secondary electrons in the sheaths (see the works of Waskoenig and Gans[40]).

The effect on the ion energy distribution function IEDF at the RF electrode is shown in Fig.5c. Again, the agreement between the standard and the different sparse PIC algorithms is very good. In a collisionless RF regime, the shape of the IEDF depends on the ratio of two parameters, namely the ion transit time $\tau_{\rm ion}$ (the time the ions spend in the discharge before being extracted) and the period of the RF field $\tau_{\rm RF}$ (see 41 and references therein). For dual-frequency capacitive discharges, $\tau_{\rm RF}$ is associated with $\tau_{\rm LF}$. The ion-neutral collisions can modify the IEDF shape, especially when the time between two collisions is $\tau_{\rm coll} < \tau_{\rm LF}$, as in CASE A. Fig.5c shows a shape with different peaks at specific energies. The same results have already been reported and analyzed in the literature[42]. The reason is that the time for the ions to reach the electrodes is greater than the inverse of the ion-neutral charge-exchange collision frequency[12]. The anisotropic backscattering process that dominates the ion-neutral collision mechanisms in the sheath induces a reduction of the energy of the primary ions to almost zero. They are accelerated again, but do not experience the full potential drop before reaching the electrodes. It is found that the number of peaks is roughly proportional to $\tau_{\rm ion}/\tau_{\rm RF}$[43]. By increasing the RF voltage to reduce the time for the ions to reach the electrodes, while keeping all other parameters fixed, Donko *et al.* in Ref.12 has shown a reduction in the number and amplitude of the peaks (a numerical study and a refined analysis of the influence of pressure and frequency on the IEDF but for a single frequency can be found in Ref. 44).

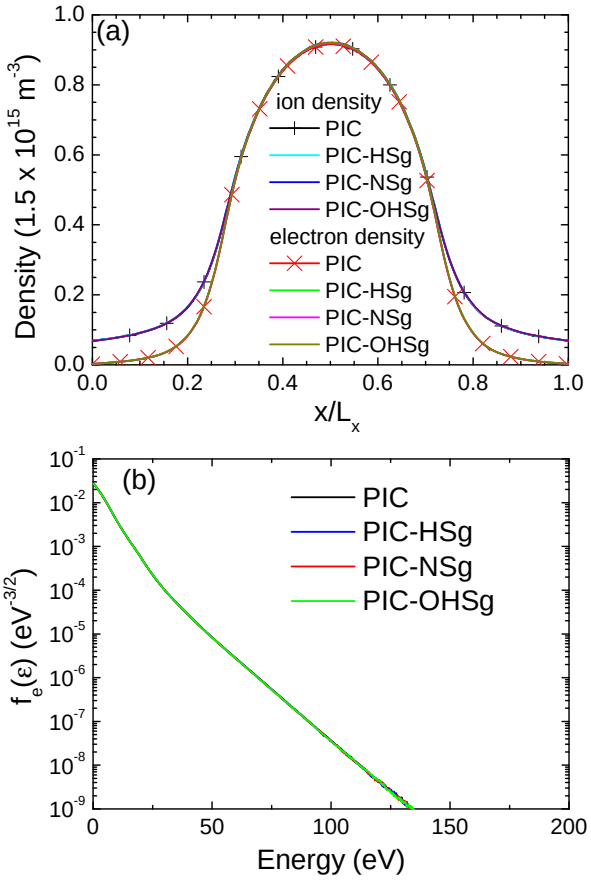

FIG. 4. Comparison of four algorithm results for CASE A. (a) Time-averaged axial profiles of electron and ion densities at mid-distance along y, (b) Time-and space-averaged electron energy probability function normalized such that $\int_0^\infty \sqrt{\varepsilon} f_e(\varepsilon)\, d\varepsilon = 1$ (semi-log scale). Standard PIC results correspond to 256^2 grid nodes. Sparse PIC results correspond to the level $n = 8$, the results of the offset method corresponds to $l^0 = 3$, and $l^1 = 1$.

B. CASE B

We have performed calculations for a higher HF frequency. By increasing the high frequency component f_{HF}, the heating mechanism of the electrons becomes more efficient. We have reduced the HF and LF excitation voltages and the neutral density to maintain a plasma density on the order of that of CASE A. This is a way to compare the standard and sparse PIC approaches also under conditions where the sheath oscil-

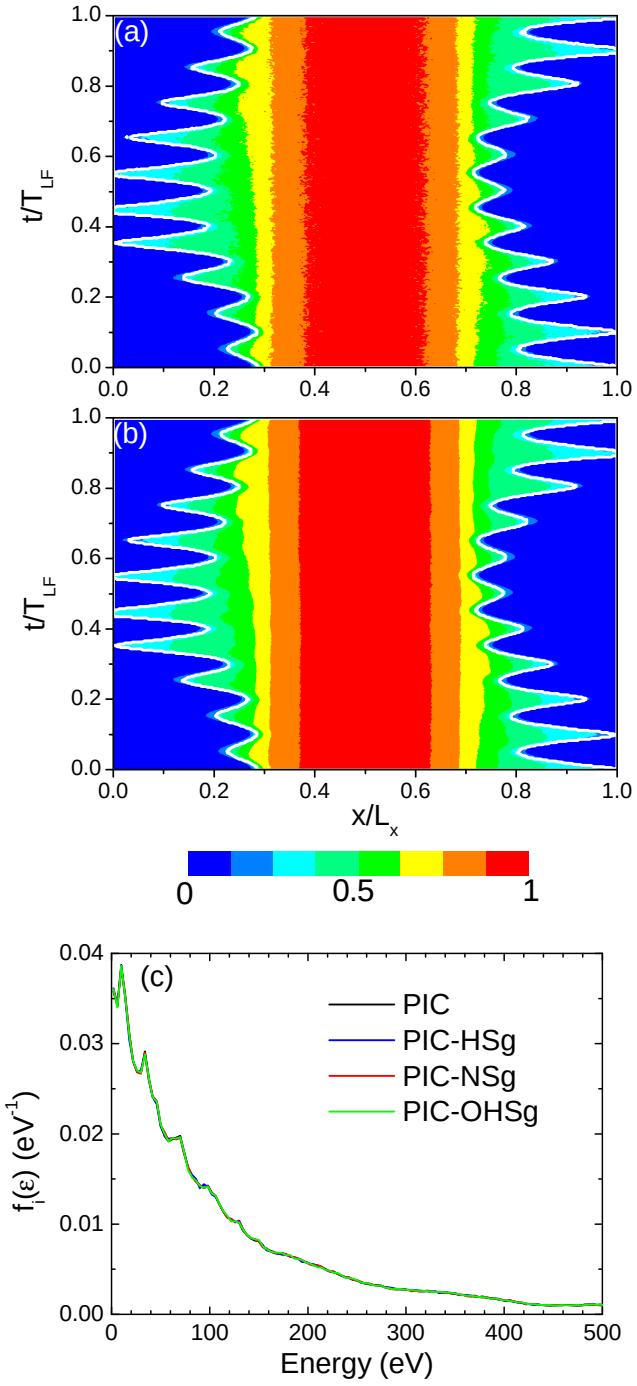

FIG. 5. CASE A. Axial and time (one LF cycle reconstructed after averaging over 60 LF cycles results after convergence) profiles of the ionization source term and sheath edge for (a) PIC and (b) PIC-HSg algorithms, (c) Time averaged ion energy probability function at the RF electrode normalized such that $\int_0^\infty f_i(\varepsilon)\,d\varepsilon = 1$. The maximum of the ionization source term is 1.6×10^{20} m^{-3} s^{-1}. Standard PIC results correspond to 256^2 grid nodes. Sparse PIC results correspond to $n = 8$, the results of the offset method corresponds to $l^0 = 3$, and $l^1 = 1$.

lations take place on a shorter time. For each calculation case, the number of particles per cell is $N_{pc} = 130$ and the total number N_T is 8.4×10^6, 8.4×10^5, 8.4×10^5, and 1.66×10^6 for the PIC, PIC-HSg, PIC-NSg, and PIC-OHSg schemes, respectively. The figure 6a shows the time averaged profiles along x at the mid distance along y of the charged particle densities. Again, the agreement between the PIC-HSg, PIC-NSg, and PIC-OHSg methods is excellent. The use of the offset algorithm for the hierarchical algorithm does not reduce the error, which is very small. The comparison of the EEDF in the same format as for CASE A is also very good (see Fig.6b). The shape of the EEDF is more complex than the previous case and the reasons for this are due to complicated and coupled mechanisms. In short, the non-local mechanism responsible for the heating of the electrons and the existence of a super-tail of high-energy electrons is still present, but for higher electron energies. For electron energies in the range of 30 – 70 eV, the inelastic processes play a role (this is visible at intermediate electron energies with the depression of the EEDF).

The space and time profiles of the ionization source and the sheath edge are shown in Fig.7a and 7b for the PIC and PIC-NSg algorithms. The modulation of the sheath edge and the ionization profile are following the fast component of the RF frequency, while the variations of the sheath thickness are of the same order as in the previous case. Again, the agreement between the two methods is very good.

The figure 7 c shows the IEDF displayed at the RF electrode and integrated over time. The very complex shape with two main peaks of large amplitude as well as the peaks of smaller amplitude are well captured with the sparse PIC schemes. The conditions of CASE B correspond to what the authors of the literature call an "intermediate" regime between a purely capacitive ($\tau_{\rm ion}/\tau_{\rm LF} >> 1$) and a purely resistive ($\tau_{\rm ion}/\tau_{\rm LF} << 1$) regime[6]. These special conditions result from the reduction of both HF and LF voltages and the increase of LF. The ion transit time is shorter than the reciprocal LF period. As the ions cross the sheath, they also feel the influence of the HF potential. The resulting effect of both frequencies shows a high energy peak close to eV_{LF} and a low energy peak a few tens of V below eV_{HF} (averaged sheath potential during an RF cycle). The secondary peaks of smaller amplitude are due to ion-neutral collisions. The same trends have been reported and extensively studied by numerical simulations[6,12,14] and experiments[45–47].

C. Discussion

According to Refs. 23, 25, and 28, the accuracy of the solutions obtained with the sparse PIC approaches is estimated by the L2-norm error quantities given by:

$$\varepsilon(\varphi) = \frac{\|\varphi - \varphi_{\rm ref}\|_{L^2}}{\|\varphi_{\rm ref}\|_{L^2}} = \sqrt{\frac{\int |\varphi - \varphi_{\rm ref}|^2 {\rm du}}{\int |\varphi_{\rm ref}|^2 {\rm du}}} \qquad (5)$$

In (5), φ and $\varphi_{\rm ref}$ are quantities (densities and distribution functions) referring to the sparse and standard PIC schemes, respectively. The integrals are taken along the x direction for

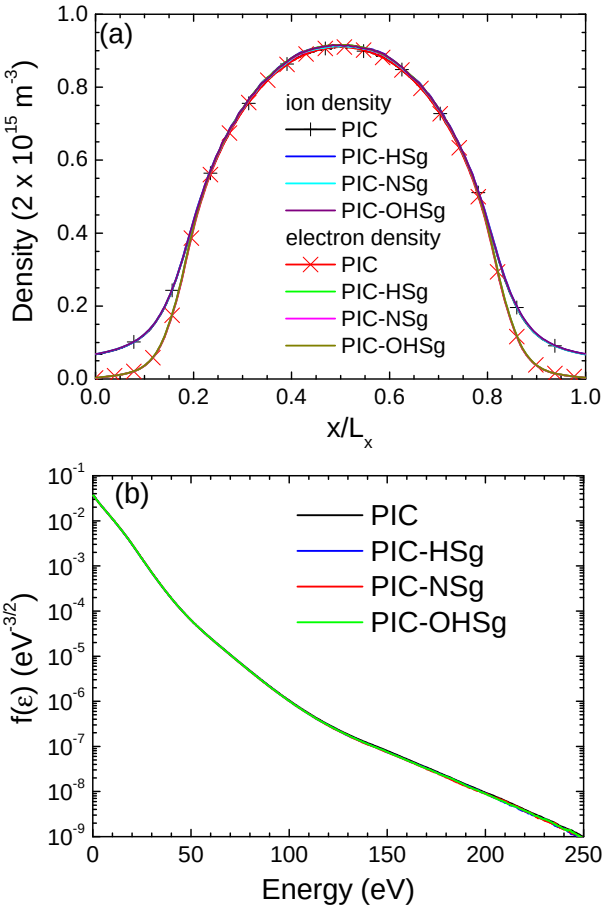

FIG. 6. Comparison of four algorithm results for CASE B. (a) Time-averaged axial profiles of electron and ion densities at mid-distance along y, (b) Time-and space-averaged electron energy probability function normalized such that $\int_0^\infty \sqrt{\varepsilon} f_e(\varepsilon)\, d\varepsilon = 1$ (semi-log scale). Standard PIC results correspond to 256^2 grid nodes. Sparse PIC results correspond to the level $n = 8$, the results of the offset method corresponds to $l^0 = 3$, and $l^1 = 1$.

one-dimensional profiles and along the x and y directions for 2D results, and over energies for distribution functions. The error calculation for all calculation cases is summarized in the table II.

For CASE A, the excellent agreement observed when comparing the profiles between standard and sparse PIC schemes is confirmed when calculating the error, which is less than 0.5 %. The error is slightly reduced with the PIC-NSg algorithm, which consists of using the nodal basis to recombine the electric potential on the regular Cartesian grid, then differentiating the electric field on the Cartesian grid, and finally calculating the electric field at the particle location as in the standard PIC algorithm (rather than recombining the electric field at the particle location without any calculations on the Cartesian grid for the PIC-HSg scheme). According to the numerical analysis detailed in Refs. 22 and 46, the off-axis contribution of the grid error is reduced by differentiating the electric field (or solving the Poisson equation) on the Cartesian grid instead of the component grids, especially for configurations where the

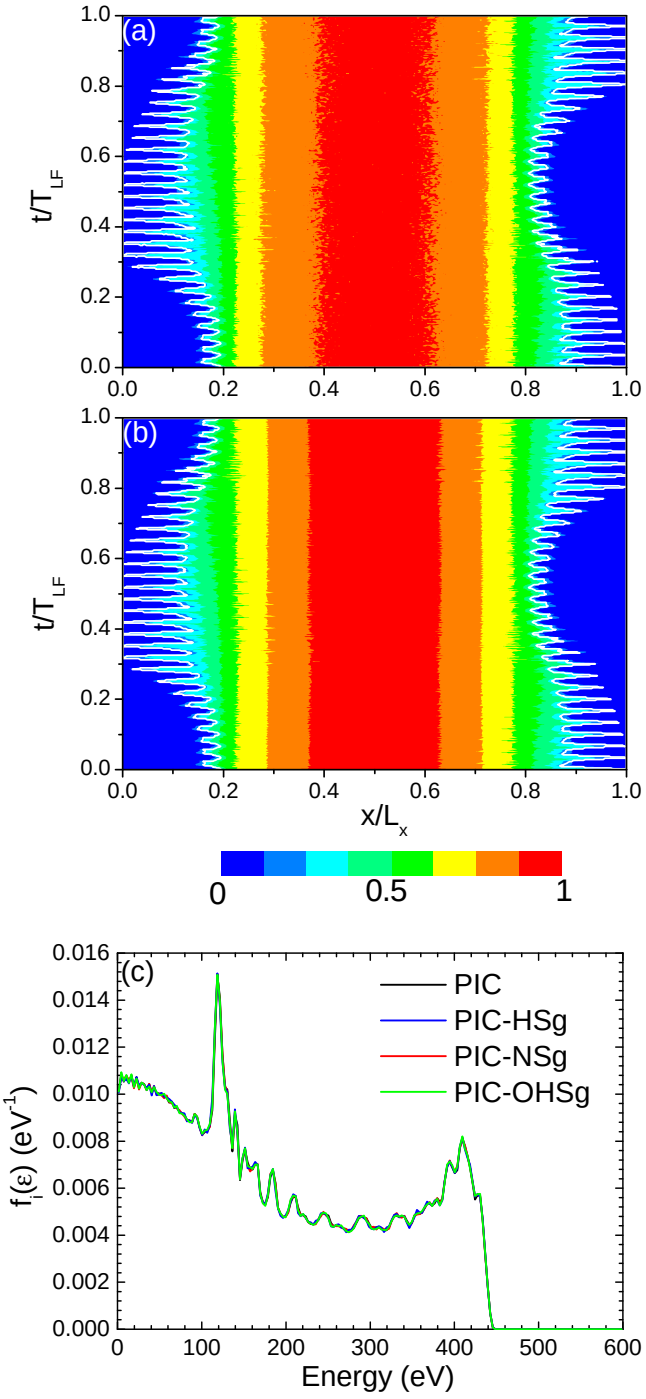

FIG. 7. CASE B. Axial and time (one LF cycle reconstructed after averaging over 60 LF cycles results after convergence) profiles of the ionization source term and sheath edge for (a) PIC and (b) PIC-NSg algorithms, (c) Time averaged ion energy probability function at the RF electrode normalized such that $\int_0^\infty f_i(\varepsilon)\, d\varepsilon = 1$. The maximum of the ionization source term is 3.4×10^{20} m^{-3} s^{-1}. Standard PIC results correspond to 256^2 grid nodes. Sparse PIC results correspond to $n = 8$, the results of the offset method corresponds to $l^0 = 3$, and $l^1 = 1$.

gradients of the solution are strong. We note that the use of the offset method does not have a strong effect on the results.

The error is slightly larger for CASE B regardless of the sparse PIC scheme, but it remains less than 1 %. We have performed longer computations, averaging the results over 100 cycles, and the results remain the same. As for CASE A, the benefit of using the offset method is marginal. We have also tested the sparse PIC algorithm when a rectangular computational domain is employed, as illustrated in Fig. 2. We have considered a simulation domain with $L_y = 4\ L_x$ corresponding to a number of grid nodes of 256×1024 in the standard PIC algorithm (with $n_1 = 8$ and $n_2 = 10$ in the sparse PIC approach). Conditions are very close to CASE A. We obtain a a small increase in the error, but the results are still in good agreement with the standard PIC approach (2 % of error).

A general observation is that electron and ion density profiles are computed using recombination techniques (and the associated grid-based error), while the charged particle distribution functions are computed directly from the phase space of the particles, and no approximation is made to compute them. Very interestingly, the ability of sparse PIC approaches, whatever the method and conditions, to capture the complex shape of the distribution functions, both for electrons and ions, is clearly demonstrated (the error is always very small, less than a few %).

Another important result is the different statistical error when using the same number of particles per cell in standard and sparse PIC schemes. We see that the level fluctuations are higher for the standard PIC approach (comparing for example the time-averaged profiles of the ionization source term of Figs.5ab and 7ab). This implies that a lower number of particles per cell can certainly be used for the sparse PIC algorithms for the same particle sampling error. This result is consistent with the recent work of Guillet[48]. This means that keeping the same number of particles per cell in the sparse PIC algorithms compared to standard PIC approach guarantees an upper bound on the statistical error.

We conclude this section by comparing the execution times for the different sparse PIC schemes. All computations were performed on the CALMIP supercomputer on the Olympe machine, 2 × Skylake processors per node (Intel Xeon Gold 6140, 2.30 GHz, 18 cores), with Intel compiler version 18.2.199 and IntelMPI version 18.2. The speed-up factor is listed in the table III. The advantage of using the PIC-NSg algorithm can be seen when comparing CASE A and CASE B due to the efficient method used to switch from hierarchical to nodal basis (and vice versa) to recombine the potential profile from the calculation on the component grids. The use of the offset method improves the results but increases the computational time because the total number of particles increases for the same statistics. The reduction of the execution time factor for CASE B is partly due to the time spent in the Monte Carlo procedure to handle collisions (20 % compared to 12 %). We also note that the PIC-HSg method is now more efficient in terms of computational time due to the strategy of using more cores. We leave the optimization of the number of cores and processors for future studies.

TABLE II. Error calculation (%).

	PIC-HSg	PIC-NSg	PIC-OHSg
CASE A			
ion density n_i	0.5	0.22	0.45
electron density n_e	0.45	0.27	0.43
EEDF	0.03	0.09	0.03
IEDF	0.14	0.11	0.1
CASE B			
ion density n_i	1	0.5	0.9
electron density n_e	1	0.4	0.9
EEDF	0.08	0.08	0.06
IEDF	0.15	0.1	0.1

TABLE III. Execution time acceleration factor (ratio of time using the standard PIC to the sparse PIC schemes)

	PIC-HSg	PIC-NSg	PIC-OHSg
CASE A (72 cores)	1.8	1.9	1.6
CASE B (72 cores)	1.6	1.8	1.4

V. CONCLUSIONS

In this paper we have used a method recently introduced in the literature whose advantage is to reduce the computational cost of PIC simulations based on sparse grids. From the initial *regular grid* with a constant mesh width, a given number of anisotropic subgrids with coarser resolution, called *component grid*, is first introduced. For any macroscopic unknown, by combining the solution from the partial solution of each of the component grids, one can approximate the unknown with a marginal increase in the grid-based error associated with the discretization. The advantage of this method is the reduction of the statistical error, which leads to a reduction of the total number of particles for the same statistical noise as the standard PIC scheme. Also, the number of nodes is reduced and the computation time to solve the Poisson's equation is reduced, accordingly. In the literature, this algorithm has been derived for a square Cartesian grid with the same number of grid nodes in all directions. We have proposed an extension of the algorithm to include the case of a rectangular computational domain with different numbers of grid nodes in each direction (while maintaining a constant mesh width).

We have tested two algorithms based on a different way to interpolate the electric field at the particle location. In both algorithms, the charged particle densities are assigned to the component grid nodes and Poisson's equation is solved on each of the component grids. In PIC-HSg, for the hierarchical sparse PIC scheme, the electric field is computed at the grid nodes of each of the component grids and interpolated at the particle location using the so-called combination tech-

nique. In PIC-NSg, for the nodal sparse PIC scheme, the combination technique is used to calculate the electric potential at the regular grid nodes from the electric potential calculated at each of the component grids. The electric field at the particle location is then interpolated from the electric field computed at the nodes of the regular grid. We have also revisited the offset scheme that has been proposed to reduce the error associated with the non-full cancellation of the error when applying the combination technique (grid-based error). The offset scheme can potentially be applied to both hierarchical and nodal sparse PIC algorithms.

The goal of this work was to demonstrate the ability of sparse PIC schemes to capture the complex and rich physics in the domain of low-temperature plasma discharges. The dual-frequency capacitive discharges provide a perfect context to test the sparse PIC schemes because the sheath and the associated charged particle density gradients vary in both space and time. We have modeled various input conditions and show that the solution is very close to the standard PIC approach (with an error of less than 2.5%). The PIC-HSg provides a slightly degraded solution. For this particular scheme, we tested the offset approach (PIC-OHSg). This scheme improves the accuracy of the solution but with a very small gain. Very interestingly, the sparse PIC approaches were able to reproduce the complex shape of the charged particle distribution functions with a very high accuracy. This work reinforces the previous study of Garrigues *et al.*[28] and the interest in the method.

These results open new perspectives. We have limited our conditions to typical plasma densities on the order of 10^{15} m^{-3} to keep the number of grid nodes small enough to run simulations for reasonable computational times. Nothing in the method prevents working with higher plasma densities. On the contrary, the higher the number of grid points in the regular Cartesian grid, the higher the reduction in the number of grid points in the component grids and particles[23,24,28] for the same statistical error, and the acceleration factor for the execution time would certainly be greater than the factor of 2 seen in the simulations of this study. Also, the use of more suitable gases for the applications and the effect of secondary electron emission under ion impacts on the electrodes[49] as well as more complex RF voltage waveforms[50] can be introduced in sparse PIC schemes without any additional complexity.

ACKNOWLEDGMENTS

M. Chung-To-Sang benefits from an Ecole Normale Supérieure - Paris Saclay PhD grant (allocation CDSN). C. Guillet benefits from a PhD grant of the Université de Toulouse Midi-Pyrénées-Région Occitanie (allocation ALDOCT-001123). This work was granted access to the HPC resources of CALMIP supercomputing center under the allocation 2013-P1125. This work is funded by l'Agence Nationale de la Recherche (ANR) under the projet ANR-22-CE46-0012. Part of has been carried out within the framework of the EUROfusion Consortium, funded by the European Union via the Euratom Research and Training Programme (Grant Agreement No 101052200 — EUROfusion). Views and opinions expressed are however those of the author(s) only and do not necessarily reflect those of the European Union or the European Commission. Neither the European Union nor the European Commission can be held responsible for them.

AUTHOR DECLARATIONS

Conflict of interest

The authors have no conflicts to disclose

Author Contributions

L. Garrigues: Conceptualization (lead); Data curation (lead); Formal analysis (equal); Funding acquisition (equal); Investigation (equal); Methodology (equal); Project administration (lead); Resources (equal); Software (equal); Supervision (lead); Validation (lead); Visualization (lead); Writing – original draft (lead); Writing – review & editing (equal). **M. Chung-To-Sang:** Conceptualization (supporting); Formal analysis (equal); Investigation (equal); Methodology (equal); Resources (equal); Supervision (equal); Validation (equal); Visualization (supporting); Writing – review & editing (equal). **G. Fubiani:** Conceptualization (supporting); Data curation (supporting); Formal analysis (equal); Funding acquisition (equal); Investigation (equal); Methodology (equal); Project administration (equal); Resources (equal); Software (equal); Supervision (equal); Validation (equal); Visualization (supporting); Writing – review & editing (equal). **C. Guillet:** Formal analysis (equal); Investigation (equal); Methodology (equal); Supervision (equal); Validation (equal); Visualization (supporting); Writing – review & editing (equal). **F. Deluzet:** Formal analysis (equal); Funding acquisition (equal); Investigation (equal); Methodology (equal); Project administration (equal); Software (equal); Supervision (equal); Validation (equal); Visualization (supporting); Writing – review & editing (equal). **J. Narski:** Formal analysis (equal); Funding acquisition (equal); Investigation (equal); Methodology (equal); Project administration (equal); Software (equal); Supervision (equal); Validation (equal); Visualization (supporting); Writing – review & editing (equal).

DATA AVAILABILITY

The data that support the findings of this study are available from the corresponding author upon reasonable request.

REFERENCES

[1] J. W. Coburn, "Some fundamental aspects of plasma-assisted etching," in *Handbook of Advanced Plasma Processing Techniques*, edited by R. J. Shul and S. J. Pearton (Springer Berlin Heidelberg, Berlin, Heidelberg, 2000) pp. 1–32.

[2] M. A. Lieberman and A. J. Lichtenberg, "Capacitive discharges," in *Principles of Plasma Discharges and Materials Processing* (John Wiley & Sons, Ltd, 2005) Chap. 11, pp. 387–460, https://onlinelibrary.wiley.com/doi/pdf/10.1002/0471724254.ch11.

[3] P. Chabert and N. Braithwaite, *Physics of Radio-Frequency Plasmas*, 1st ed. (Cambridge University Press, Cambridge, UK, 2011).

[4] J. K. Lee, O. V. Manuilenko, N. Y. Babaeva, H. C. Kim, and J. W. Shon, "Ion energy distribution control in single and dual frequency capacitive plasma sources," Plasma Sources Science and Technology **14**, 89 (2005).

[5] P. C. Boyle, A. R. Ellingboe, and M. M. Turner, "Independent control of ion current and ion impact energy onto electrodes in dual frequency plasma devices," Journal of Physics D: Applied Physics **37**, 697 (2004).

[6] P. C. Boyle, A. R. Ellingboe, and M. M. Turner, "Electrostatic modelling of dual frequency rf plasma discharges," Plasma Sources Science and Technology **13**, 493 (2004).

[7] Z. Bi, Y. Liu, W. Jiang, X. Xu, and Y. Wang, "A brief review of dual-frequency capacitively coupled discharges," Current Applied Physics **11**, S2–S8 (2011).

[8] E. Kawamura, M. A. Lieberman, and A. J. Lichtenberg, "Stochastic heating in single and dual frequency capacitive discharges," Physics of Plasmas **13**, 053506 (2006), https://doi.org/10.1063/1.2203949.

[9] K. Denpoh and K. Nanbu, "Self-consistent particle simulation of radio-frequency CF_4 discharge with implementation of all ion-neutral reactive collisions," Journal of vacuum science & technology A **16**, 1201–1206 (1998).

[10] V. Georgieva and A. Bogaerts, "Plasma characteristics of an $Ar/CF_4/N_2$ discharge in an asymmetric dual frequency reactor: numerical investigation by a PIC/MC model," Plasma Sources Science and Technology **15**, 368 (2006).

[11] J. Schulze, Z. Donkó, E. Schüngel, and U. Czarnetzki, "Secondary electrons in dual-frequency capacitive radio frequency discharges," Plasma Sources Science and Technology **20**, 045007 (2011).

[12] Z. Donkó, A. Derzsi, M. Vass, B. Horváth, S. Wilczek, B. Hartmann, and P. Hartmann, "eduPIC: an introductory particle based code for radio-frequency plasma simulation," Plasma Sources Science and Technology **30**, 095017 (2021).

[13] G. Wagayama and K. Nanbu, "Study on the dual frequency capacitively coupled plasmas by the Particle-in-Cell/Monte Carlo method," IEEE Transactions on Plasma Science **31**, 638–644 (2003).

[14] S. Rauf, P. Tian, J. Kenney, and L. Dorf, "Effect of low frequency voltage waveform on plasma uniformity in a dual-frequency capacitively coupled plasma," Journal of Vacuum Science & Technology B **40**, 032202 (2022), https://doi.org/10.1116/6.0001732.

[15] H. Wang, W. Jiang, and Y. Wang, "Parallelization and optimization of electrostatic particle-in-cell/monte-carlo coupled codes as applied to rf discharges," Computer Physics Communications **180**, 1305–1314 (2009).

[16] H. Wang, W. Jiang, and Y. Wang, "Implicit and electrostatic particle-in-cell/monte carlo model in two-dimensional and axisymmetric geometry: I. Analysis of numerical techniques," Plasma Sources Science and Technology **19**, 045023 (2010).

[17] J. S. Kim, M. Y. Hur, C. H. Kim, H. J. Kim, and H. J. Lee, "Advanced PIC-MCC simulation for the investigation of step-ionization effect in intermediate-pressure capacitively coupled plasmas," Journal of Physics D: Applied Physics **51**, 104004 (2018).

[18] J. Shin, H. Kim, and H. Lee, "Two-dimensional particle-in-cell simulation parallelized with graphics processing units for the investigation of plasma kinetics in a dual-frequency capacitively coupled plasma," Reviews of Modern Plasma Physics **6**, 30 (2022).

[19] C. K. Birdsall and A. B. Langdon, *Plasma physics via computer simulation* (Taylor and Francis, New York, 2005).

[20] R. W. Hockney and J. W. Eastwood, *Computer simulation using particles* (Bristol: Hilger, 1988).

[21] A. Langdon, "Effects of the spatial grid in simulation plasmas," Journal of Computational Physics **6**, 247–267 (1970).

[22] A. T. Powis and I. D. Kaganovich, "Accuracy of the explicit energy-conserving particle-in-cell method for under-resolved simulations of capacitively coupled plasma discharges," Physics of Plasmas **31**, 023901 (2024), https://pubs.aip.org/aip/pop/article-pdf/doi/10.1063/5.0174168/19725114/023901_1_5.0174168.pdf.

[23] L. F. Ricketson and A. J. Cerfon, "Sparse grid techniques for particle-in-cell schemes," Plasma Physics and Controlled Fusion **59**, 024002 (2016).

[24] F. Deluzet, G. Fubiani, L. Garrigues, C. Guillet, and J. Narski, "Sparse grid reconstructions for Particle-In-Cell methods," ESAIM: M2AN **56**, 1809–1841 (2022).

[25] F. Deluzet, G. Fubiani, L. Garrigues, C. Guillet, and J. Narski, "Efficient parallelization for 3D-3V sparse grid Particle-in-Cell: shared memory systems architectures," Journal of Computational Physics **480**, 112022 (2023).

[26] F. Deluzet, G. Fubiani, L. Garrigues, C. Guillet, and J. Narski, "Efficient parallelization for 3d-3v sparse grid Particle-In-Cell: Single GPU architectures," Computer Physics Communications **289**, 108755 (2023).

[27] S. Muralikrishnan, A. J. Cerfon, M. Frey, L. F. Ricketson, and A. Adelmann, "Sparse grid-based adaptive noise reduction strategy for particle-in-cell schemes," Journal of Computational Physics: X **11**, 100094 (2021).

[28] L. Garrigues, B. Tezenas du Montcel, G. Fubiani, F. Bertomeu, F. Deluzet, and J. Narski, "Application of sparse grid combination techniques to low temperature plasmas Particle-In-Cell simulations. I. Capacitively coupled radio frequency discharges," Journal of Applied Physics **129**, 153303 (2021), https://doi.org/10.1063/5.0044363.

[29] L. Garrigues, B. Tezenas du Montcel, G. Fubiani, and B. C. G. Reman, "Application of sparse grid combination techniques to low temperature plasmasParticle-In-Cell simulations. II. Electron drift instability in a hall thruster," Journal of Applied Physics **129**, 153304 (2021), https://doi.org/10.1063/5.0044865.

[30] Y. N. Grigoryev, V. A. Vshivkov, and M. P. Fedoruk, *Numerical Particle-in-Cell Methods: Theory and Applications* (Walter de Gruyter, Boston, 2002).

[31] J. P. Verboncoeur, "Particle simulation of plasmas: review and advances," Plasma Physics and Controlled Fusion **47**, A231 (2005).

[32] J. P. Boris, "Relativistic plasma simulation - optimization of a hybrid code," in *Proc. 4th Conference on the Numerical Simulation of Plasmas*, edited by J. P. Boris and R. A. Shanny (Office of Naval Research, Arlington, VA, 1970) p. 3.

[33] LXCat, "Biagi-v7.1 database," (2023), `https://www.lxcat.net/`. retrieved on February 15, 2023.

[34] M. M. Turner, A. Derzsi, Z. Donkó, D. Eremin, S. J. Kelly, T. Lafleur, and T. Mussenbrock, "Simulation benchmarks for low-pressure plasmas: Capacitive discharges," Physics of Plasmas **20**, 013507 (2013), https://doi.org/10.1063/1.4775084.

[35] A. V. Phelps, "The application of scattering cross sections to ion flux models in discharge sheaths," Journal of Applied Physics **76**, 747–753 (1994), https://doi.org/10.1063/1.357820.

[36] V. A. Godyak and R. B. Piejak, "Abnormally low electron energy and heating-mode transition in a low-pressure argon rf discharge at 13.56 MHz," Physical Review Letters **65**, 996–999 (1990).

[37] V. A. Godyak, R. B. Piejak, and B. M. Alexandrovich, "Measurement of electron energy distribution in low-pressure rf discharges," Plasma Sources Science and Technology **1**, 36 (1992).

[38] V. A. Godyak, R. B. Piejak, and B. M. Alexandrovich, "Evolution of the electron-energy-distribution function during rf discharge transition to the high-voltage mode," Phys. Rev. Lett. **68**, 40–43 (1992).

[39] V. A. Godyak, R. B. Piejak, and B. M. Alexandrovich, "Effective electron collision frequency and electrical conductivity of radio frequency plasmas," Journal of Applied Physics **85**, 3081–3083 (1999), https://pubs.aip.org/aip/jap/article-pdf/85/6/3081/10596966/3081_1_online.pdf.

[40] J. Waskoenig and T. Gans, "Nonlinear frequency coupling in dual radio-frequency driven atmospheric pressure plasmas," Applied Physics Letters **96** (2010), 10.1063/1.3425668, 181501, https://pubs.aip.org/aip/apl/article-pdf/doi/10.1063/1.3425668/14430830/181501_1_online.pdf.

[41] D. Gahan, S. Daniels, C. Hayden, P. Scullin, D. O'Sullivan, Y. T. Pei, and M. B. Hopkins, "Ion energy distribution measurements in rf and pulsed dc plasma discharges," Plasma Sources Science and Technology **21**, 024004 (2012).

[42]E. Schüngel, Z. Donkó, and J. Schulze, "A simple model for ion flux-energy distribution functions in capacitively coupled radio-frequency plasmas driven by arbitrary voltage waveforms," Plasma Processes and Polymers **14**, 1600117 (2017), https://onlinelibrary.wiley.com/doi/pdf/10.1002/ppap.201600117.

[43]E. Kawamura, V. Vahedi, M. A. Lieberman, and C. K. Birdsall, "Ion energy distributions in rf sheaths; review, analysis and simulation," Plasma Sources Science and Technology **8**, R45 (1999).

[44]M. Surendra and D. Graves, "Particle simulations of radio-frequency glow discharges," IEEE Transactions on Plasma Science **19**, 144–157 (1991).

[45]T. V. Rakhimova, O. V. Braginsky, V. V. Ivanov, A. S. Kovalev, D. V. Lopaev, Y. A. Mankelevich, M. A. Olevanov, O. V. Proshina, A. T. Rakhimov, A. N. Vasilieva, and D. G. Voloshin, "Experimental and theoretical study of ion energy distribution function in single and dual frequency rf discharges," IEEE Transactions on Plasma Science **35**, 1229–1240 (2007).

[46]Z.-C. Li, D.-L. Chang, X.-S. Li, Z.-H. Bi, W.-Q. Lu, Y. Xu, A.-M. Zhu, and Y.-N. Wang, "Experimental investigation of ion energy distributions in a dual frequency capacitively coupled Ar/CF4 plasma," Physics of Plasmas **17** (2010), 10.1063/1.3304186, 033501, https://pubs.aip.org/aip/pop/article-pdf/doi/10.1063/1.3304186/14818548/033501_1_online.pdf.

[47]J. Liu, Q.-Z. Zhang, Y.-X. Liu, F. Gao, and Y.-N. Wang, "Measurements of ion energy distributions in a dual-frequency capacitively coupled plasma for Ar/O2 discharges," Journal of Physics D: Applied Physics **46**, 235202 (2013).

[48]C. Guillet, *Approche sur grilles parcimonieuses pour accélérer la méthode Particle-In-Cell*, Ph.D. thesis, University of Toulouse (2023).

[49]A. Derzsi, Z. Donkó, and J. Schulze, "Coupling effects of driving frequencies on the electron heating in electronegative capacitive dual-frequency plasmas," Journal of Physics D: Applied Physics **46**, 482001 (2013).

[50]T. Lafleur, "Tailored-waveform excitation of capacitively coupled plasmas and the electrical asymmetry effect," Plasma Sources Science and Technology **25**, 013001 (2015).